Supplementary Material

Supplementary Material 1. Image reconstruction details

Magnitude and phase GRE images were reconstructed offline on a 512x512x64 spatial matrix using sum-of-squares and scalar phase matching (Hammond et al., 2008), respectively. The *k*-space was zero-padded in phase-encode direction before the reconstruction to achieve an isotropic in-plane resolution. In-plane distortions due to imaging gradient non-linearity were compensated for in image space (Polak et al., 2015). Phase images were unwrapped with a best-path algorithm (Abdul-Rahman et al., 2007), background-field corrected with V-SHARP (Li et al., 2011; Schweser et al., 2011) (radius 5mm; TSVD threshold 0.05), and converted to magnetic susceptibility maps using the HEIDI algorithm (Schweser et al., 2012). Magnetic susceptibility maps were referenced (0 ppb) to the average susceptibility of the brain. This reference was chosen to minimize a potential confounding bias from (unknown) disease-related susceptibility changes in a more localized anatomical reference region (Deistung et al., 2013; Straub et al., 2016) and to minimize the impact of reconstruction artifact related variations of observed susceptibility in the reference regions on the inter-subject variations of the referenced regions.

Supplementary Material 2. Multivariate analysis with untransformed variables

The results of the multivariate analysis using untransformed variables are listed in Tables S.1 and S.2. The fastest decline in susceptibility with dd was observed in the PUL with 0.585 ppb/a, followed by the GT with more than 0.234 ppb/a. PUL and GT showed a reduction in the volume of more than 14.87 µl/a and more than 27.17 µl/a, respectively. The volume reduction in the LNR was 5.12 µl/a. The susceptibility reduction with age in the left MNR was 0.392 ppb/a, which was accompanied by a reduction in volume of 5.46 µl/a. Despite a significant linear correlation between the dd and age (r=0.65, p<0.001), the condition indices of the collinearity analyses did not exceed 13.

Supplementary Material 3. Contribution of calcium to brain susceptibility in MS

Besides iron, susceptibility changes may have other biophysical causes, such as diamagnetic calcium. While histopathological studies of the thalamus in MS are scarce and calcium is rarely assessed in routine histopathology, to the best of our knowledge, no evidence exists for calcium accumulation in MS.

We have recently carried out a Monte-Carlo simulation to explain our previous findings of decreased GT susceptibility (Hagemeier et al., 2017). Our simulations indicated that some involvement of calcium would benefit the combined explanation of the totality of published findings (Hagemeier et al., 2017). A potential hypothesis for calcification accumulation could be linked to hemodynamics. In particular, Zivadinov et al. (Zivadinov et al., 2010) reported correlations between susceptibility MRI in the PUL and venous hemodynamic parameters in MS. Posterior cerebral hyperperfusion has been implicated with dystrophic PUL calcification in Fabry disease (Charil et al., 2006; Moore et al., 2003).

Other explanations related to calcium are (i) mitochondrial impairment, which is known to be associated with excessive Ca^{2+} uptake (Cheng et al., 2012; Contreras et al., 2010) and release of insoluble calcium phosphate (Panov et al., 2004). In addition, it has been shown that MS patients with single nucleotide polymorphisms of the glutamate NMDA receptor 2A subunit showed higher brain atrophy (Strijbis et al., 2013), a subunit that has been associated with prolonged thalamic Ca^{2+} influx in traumatic brain injury (Osteen et al., 2004; Osteen et al., 2001), visible on QSM (Schweser et al., 2017); (ii) a disturbed axonal ion homeostasis in MS that leads to axonal Ca^{2+} accumulation (Lassmann et al., 2012); or (iii) calcium accumulation associated with abnormally extended thalamic burst mode, which is known to be related to sustained calcium elevation (Zhou et al., 1997). Studies suggest that PUL neurons burst more than other thalamic regions (Ramcharan et al., 2005; Wei et al., 2011) potentially due to a higher density of T-type Ca^{2+} channels in the PUL (Wei et al., 2011). Furthermore, hyperpolarizing GABAergic input to higher order nuclei such as the PUL likely predispose them to burst mode (Sherman and Guillery, 2013).

Supplementary Material 4. Technical limitations of the study

A common technical challenge in QSM-based studies is the requirement for intra-subject referencing of the susceptibility values (Feng et al., 2017; Straub et al., 2016). A negative consequence of this referencing is that it is impossible to detect pathological susceptibility alterations in the reference region. Moreover, such alterations may propagate to the referenced susceptibility values causing spurious group differences. Another negative side-effect of referencing is that the inter-subject variability of the (calculated) susceptibility in the reference region propagates to the referenced values, which increases the variation and can render group differences insignificant (decreased statistical power). In the present study, we used the brain-average susceptibility as a reference, assuming that it this value, due to the high number of voxels involved in the averaging process, is relatively insensitive to intra-subject variations.

However, although potentially counterbalanced by the loss of iron in the NAWM, global demyelination, which is known to be present in MS patients, may increase the absolute susceptibility of the whole brain, reducing the observed *referenced* susceptibility values in patients compared to controls (Feng et al., 2017). To test if the choice of the reference region is responsible for the observed reduction in thalamic susceptibility, we re-calculated the group differences using the reference regions employed in previous studies: frontal WM (Rudko et al., 2014), internal capsule (Al-Radaideh et al., 2013), and lateral ventricles (Chen et al., 2014; Harrison et al., 2016; Li et al., 2016). While considerable alterations in the group differences of the susceptibility, particularly in the WM, were observed after referencing to the different regions, the thalamic group differences were qualitatively similar to those obtained with the whole-brain reference (see Fig. S.5). It may be concluded that the choice of the reference region did not influence the overall conclusions of the present study.

Another limitation relates to the employed pulse sequence, which required a relatively long acquisition time (8 minutes) and is, hence, prone to motion artifacts. While we inspected all susceptibility maps to confirm the absence of obvious artifacts, we cannot exclude that subtle head motion, which may be more dominant in patients due to tremor or increased discomfort, affects the non-linear field-to-source inversion procedures of QSM. It is possible that the low degree of numerical regularization used in our (compressive-sensing [CS]-type) HEIDI algorithm renders the reconstruction more prone to motion artifacts than the algorithms used by Rudko (Rudko et al., 2014) et al. (who reported *increased* thalamic iron in MS). However, Burgetova et al. (Burgetova et al., 2017) and Elkady et al. (Elkady et al., 2015) found decreased GT and subregional susceptibilities with algorithms that are not of the CS-type (Bilgic et al., 2012; Langkammer et al., 2015). Similar to HEIDI, and different from the algorithm used by Langkammer and Rudko et al., Burgetova's and Elkady's algorithms did not incorporate anatomical priors derived from magnitude images. Figure S.7 compares the reconstruction accuracy of different QSM algorithm types in the thalamus, indicating systematic overestimation of thalamic susceptibility with the magnitude-informed algorithm. While the cause of this overestimation is unclear, magnitude-informed QSM may be particularly problematic in the thalamus because the thalamus is usually not clearly discernible on GRE magnitude images. Future research will need to elucidate the sensitivity of different QSM algorithms to motion and the quality of anatomical priors.

Spatial normalization inaccuracy is another confounding factor in our study. While the thalamic subnuclei were discernible in most of the subject, the thalamus appeared relatively homogeneous in others. Spatial normalization can only be accurate if the image contrast

employed for the normalization is sufficiently rich to guide the non-linear warp-field computations. In the absence of intra-thalamic contrast, only the outside boundaries of the thalamus may be used for the normalization, potentially resulting in inaccurate normalization of thalamic subnuclei. While this limitation did not affect the assessment of mean susceptibility values or the VBA, it may have increased the uncertainty of volume estimations in the present study.

Table S.1. Coefficients of the linear multivariate analysis of susceptibility in all 120 patients using untransformed variables.

Susceptibility	c_0 in ppb	c_{DD} in ppb/a	c_{Age} in ppb/a	c_{Sex} in ppb	R^2 (p^F)
GT					
Left	10.55	-0.234	-0.102	-0.731	0.22 (<0.001)
Right	11.79	-0.239†	-0.092	-1.277	0.21 (<0.001)
PUL					
Avg	33.4	-0.585†	-0.035	-1.721	0.31 (<0.001)
MNR					
Left	17.99	-0.146	-0.392†	-1.555	0.21 (<0.001)
Right	17.03	-0.327	-0.309	-3.477	0.21 (<0.001)
LNR					
Left	9.32	-0.140	-0.142	-1.019	0.16 (<0.001)
Right	10.158	-0.087	-0.126	-0.672	0.10 (0.012)

p^F is the overall p-value of the ANOVA F-test. Multivariate analysis was performed for left and right hemispheres separately if inter-hemispheric differences were observed in mean values (Tabs. 2 and 3). For the association with sex, we used 0 for female and 1 for male patients. Note that confidence intervals and *p*-values may be unreliable due to non-normal and heteroscedastic sample distributions of the untransformed variables (see text). Hence, we do not report their values here. The superscript † indicates coefficients that were statistically significant when the multivariate analysis was carried out based on transformed variables.

Table S.2. Coefficients of the linear multivariate analysis of volumes in all 120 patients using untransformed variables.

Volumes	d_0 in ml	d_{DD} in µl/a	d_{Age} in µl/a	d_{Sex} in µl	R^2 (p^F)
GT					
Left	8.777	-27.166	-21.61	28.66	0.27 (<0.001)
Right	8.650	-35.88†	-13.90	-110.0	0.28 (<0.001)
PUL					
Left	2.170	-11.777†	-3.641	21.33	0.20 (<0.001)
Right	2.221	-14.87†	-0.363	24.62	0.20 (<0.001)
MNR					
Left	0.966	-1.582	-5.457†	-7.970	0.29 (<0.001)
Right	0.989	-3.046	-4.092	-43.80	0.24 (<0.001)
LNR					
Avg	1.038	-5.119†	-0.963	-13.640	0.21 (<0.001)

p^F is the *p*-value of the ANOVA F-test. Multivariate analysis was performed for left and right hemispheres separately if inter-hemispheric differences were observed in mean values (Tabs. 2 and 3). For the association with sex, we used 0 for female and 1 for male patients. Note that confidence intervals and *p*-values may be unreliable due to non-normal and heteroscedastic sample distributions of the untransformed variables (see text). Hence, we do not report their values here. The superscript † indicates coefficients that were statistically significant when the multivariate analysis was carried out based on transformed variables.

Table S.3. Comparison of demographics and clinical characteristics in previous QSM or R_2*-based MS studies and the present work.

	Khalil 2009	**Al-Radaideh 2013**	**Langkammer 2013**	**Rudko 2014**	**Cobzas 2015**	**Khalil 2015**	**Fujiwara 2017**	**Hagemeier 2017**	**Elkady 2017**	**Burgetova 2017**	**Present study**
CIS											
Age (years)	33.9, 24.8-9.9	36.6±8.9	35.4±11.7		-	**32±8.3**	-	-	37.3±9.2	-	36.9±9.8
Sex ratio (F/M)	2.2	1.1	2.7	*combined with RRMS*[b]	-	1.9	-	-	2.2	-	2.6
EDSS	1.0, 0.0-2.4	1.74 [0-3.5]	1.2, 0-2		-	1.0, 0-2	-	-	1.7±1.4	-	1.5, 0.5-2.5
dd (years)	**0.3, 0.1-0.9**	1.45 [0.4-4.7]	**0.77±1.6**		-	**0.3, 0.1-0.7**	-	-	-	-	2.2±2.6
RRMS											
Age (years)	**37.1, 32.1-2.2**	-	**34.6±9.1**	**37.3±6.1**	**35.64 [19.5-1.4]**	**34.2±9.3**		44.2±10.2	**39.0±10.0**	46.9±7.0	43.6±10.1
Sex ratio (F/M)	1.47	-	2.0	**3.6**	**5.1**	**1.3**	*combined with SPMS*[d]	2.1	**4.7**	**0.7**	2.1
EDSS	2.0, 1.0-3.4	-	**1.0, 0-2**	1.70 [0-6]	2.35 [1-5]	2.0, 1.0-3.3		2.5, 1.5-4	2.3±.1.0	2.5, 1.25-3.75	2.0, 1-3
dd (years)	8.1, 4.2-13.3	-	**7.3±5.6**	*not specified*	**5.28 [0.7-10.7]**	7.5, 4.2-13.0		**12.8±9.4**	**6.2±4.0**	12.4±10.7	9.8±6.0
SPMS					-						
Age (years)	-	-			-		49.1±10.3		50.3±8.9	-	52.0±7.0
Sex ratio (F/M)	-	-	*combined with RRMS*[a]		-	*combined with RRMS*[c]	2.1	*combined with RRMS*[e]	**1.36**	-	2.6
EDSS	-	-			-		5.25* [2.0-9.0]		5.9±1.3	-	6.5, 4-9
dd (years)	-	-			-		**14.9±8.9**		**18.8±8.1**	-	24.0±10.2

Values stated as *n*, *m-p* represent median, IQR; *n*±*m* indicates mean and standard deviation; *n* [*m-p*] indicates mean and range; *n** [*m-p*] indicates median and range. Entries with substantial deviation from the present study are printed in **boldface**.

[a] The authors described the group as "diagnosis of MS."

[b] 84% of the patients had RRMS; other patients included in the group had a diagnosis of CIS.

[c] 81.5% of the MS patients had RRMS; other patients had SPMS.

[d] 37.5% of the patients had SPMS, 22.5% had primary progressive MS, and 40% had RRMS.

[e] 98% (81.7%) of the studied patients had RRMS at baseline (follow-up); other patients had SPMS. In this table, we report the *baseline* characteristics of the whole group.

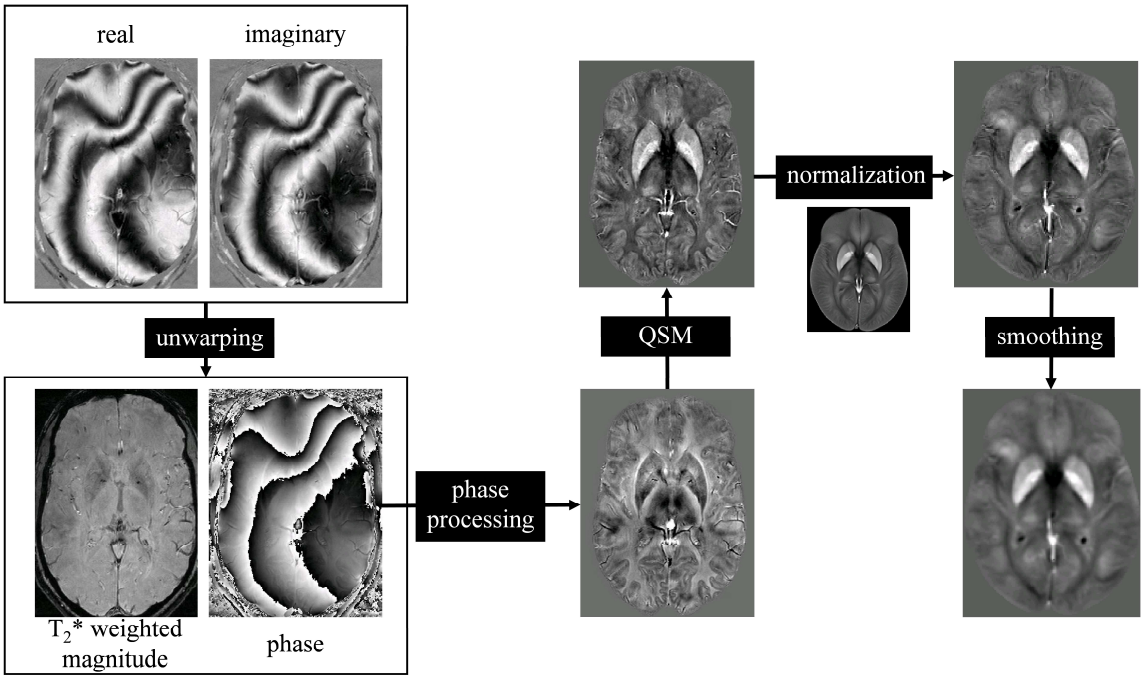

Figure S.1. Overview of the processing steps in this study. Real and imaginary images were reconstructed from raw k-space and distortions due to non-linear gradients were compensated for (unwarping). The phase images were unwrapped and background field corrected (phase processing), followed by a calculation of the susceptibility maps (QSM). The maps were spatially normalized to a custom susceptibility brain template, followed by spatial smoothing.

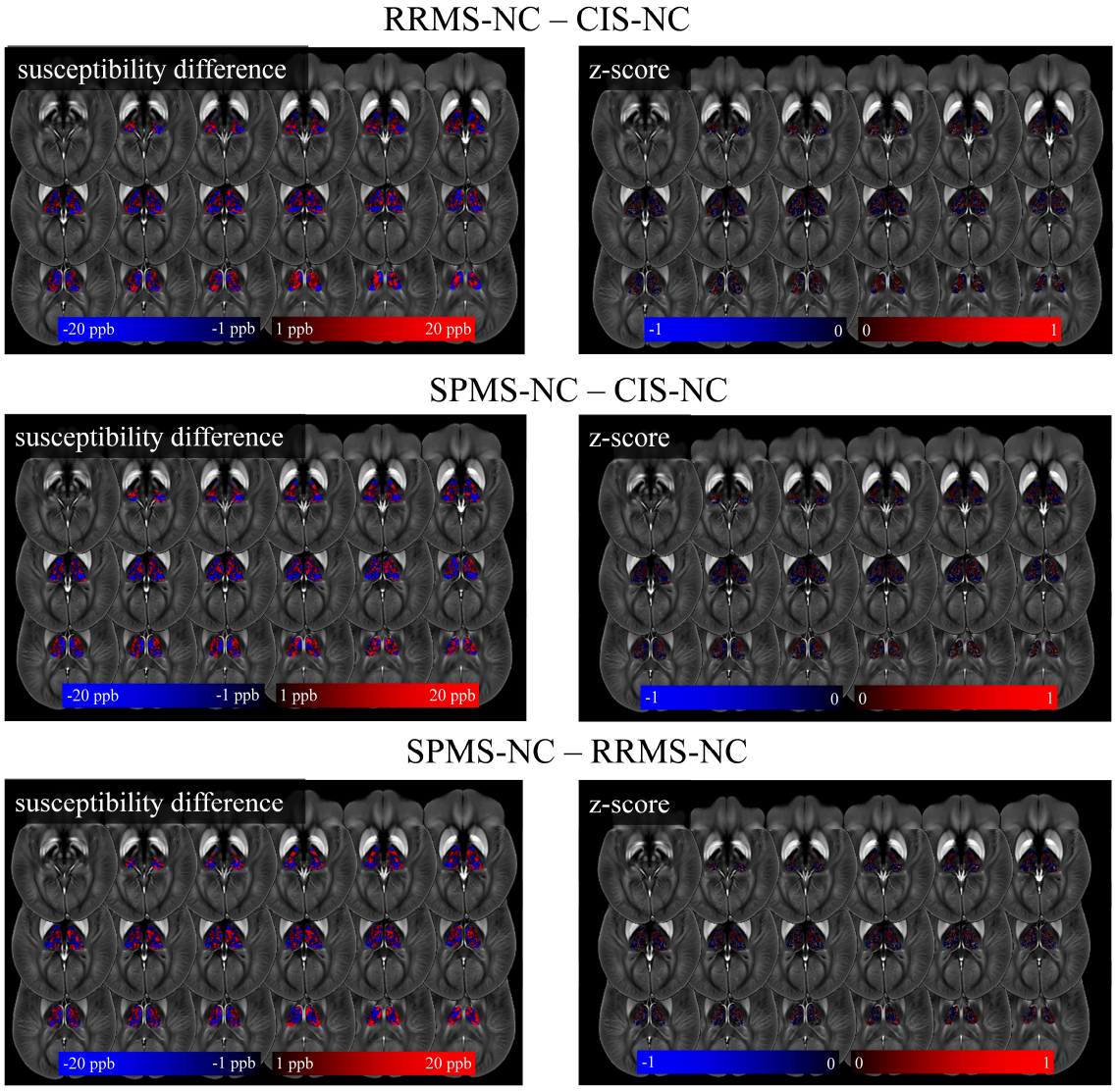

Figure S.2. Voxel-based differences of group-average magnetic susceptibility (left-hand side) and corresponding Z-scores (right-hand side) between the three control groups (top to bottom).

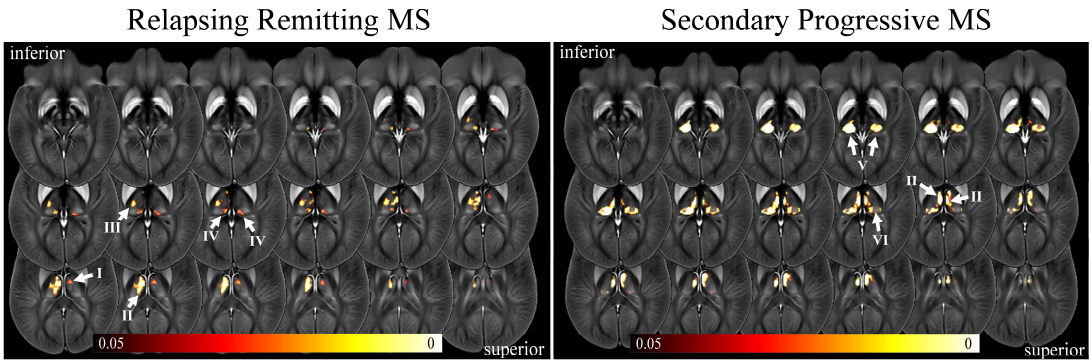

Figure S.3. Regions in which differences between patients and controls reached statistical significance. Shown are voxels with a p-value below 0.05 after TFCE.

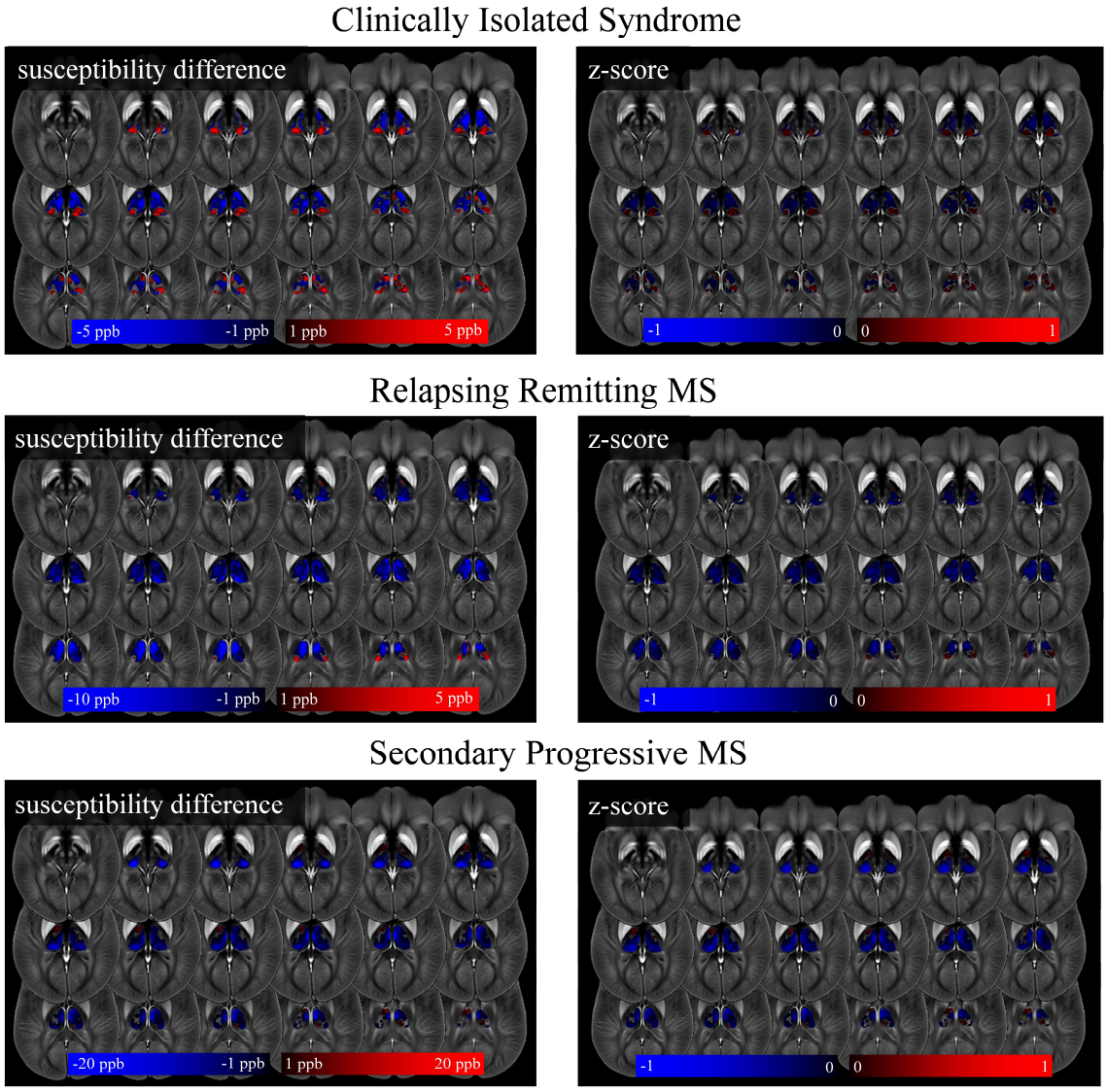

Figure S.4. Voxel-based differences between patients and controls of group-average magnetic susceptibility (left-hand side) and corresponding Z-scores (right-hand side) for all three study groups (top to bottom). Note the differences in contrast between the study groups (color bars).

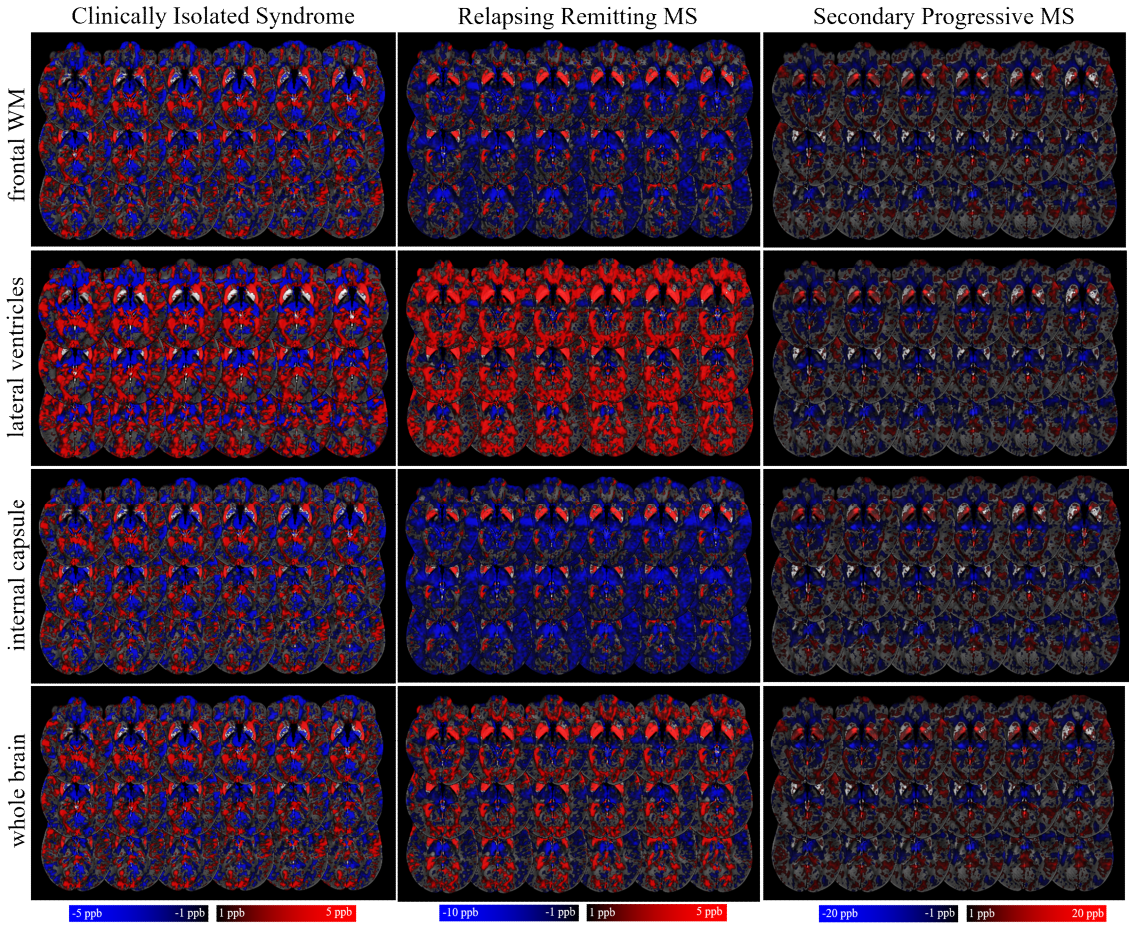

Figure S.5. The effect of the susceptibility reference region. Susceptibility differences between patient and control groups are shown in the different columns; each row used a different reference region previously employed in the literature. The Figure is analogous to Figure 2b (in particular, the contrast settings are identical), except that the difference calculation was not restricted to the thalamus. While major differences were observed in the white matter depending on the chosen reference, the general finding of reduced thalamic magnetic susceptibility did not depend on the reference region – all reference regions yielded the same qualitative results in the thalamus. All maps also showed the previously reported increased magnetic susceptibility in the basal ganglia due to increased tissue iron in patients.

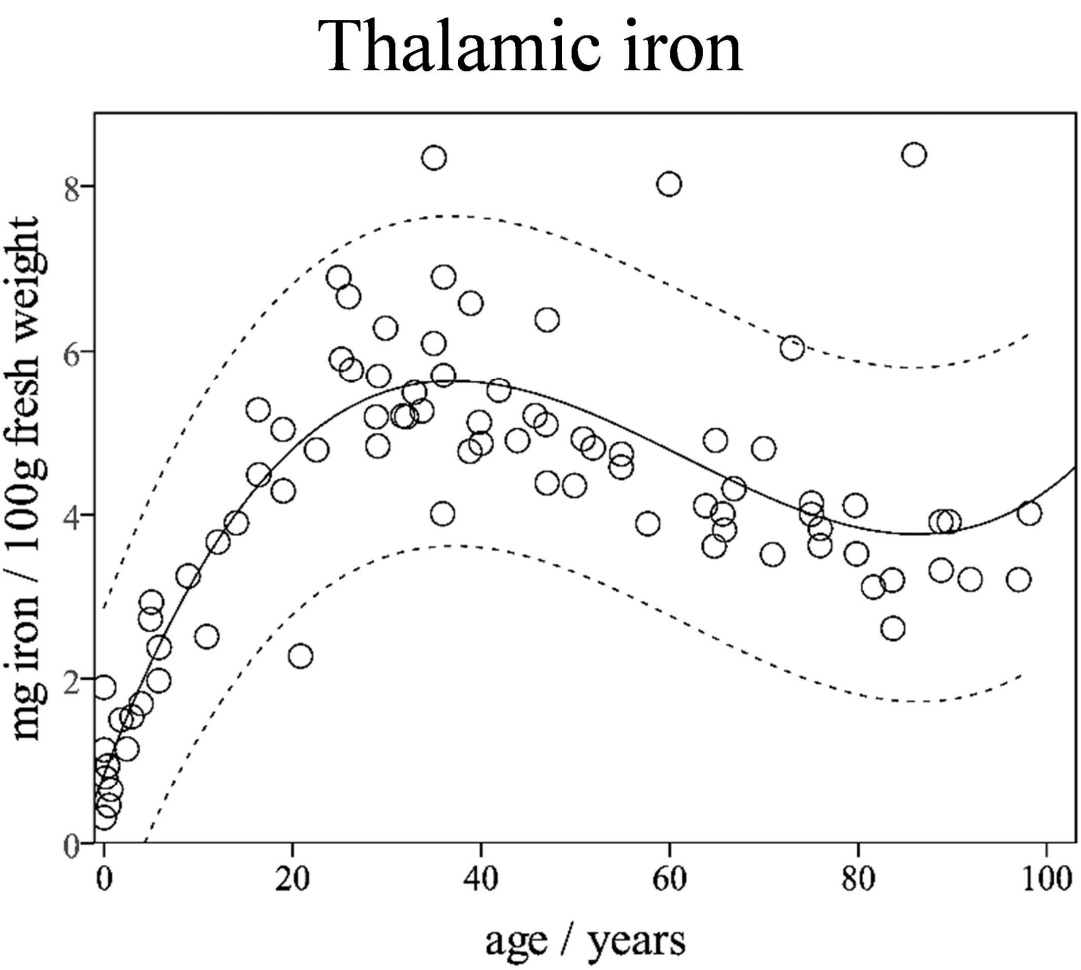

Figure S.6. Thalamic iron data reported by Hallgren and Sourander (Hallgren and Sourander, 1958). We extracted data points from the original publication using the manual mode of WebPlotDigitizer (version 3.9; Ankit Rohatgi, Austin, Texas, USA). The solid line is a cubic fit given by the following equation: (0.848±0.287) mg/100g + (0.301±0.029) mg/100g · *age* – (5.82±0.79)·10^{-3} mg/100g · age^2 + (3.150±0.60)·10^{-5} mg/100g · age^3 (R^2=0.69; all coefficients p<0.01). The dashed lines indicate the 95% confidence interval.

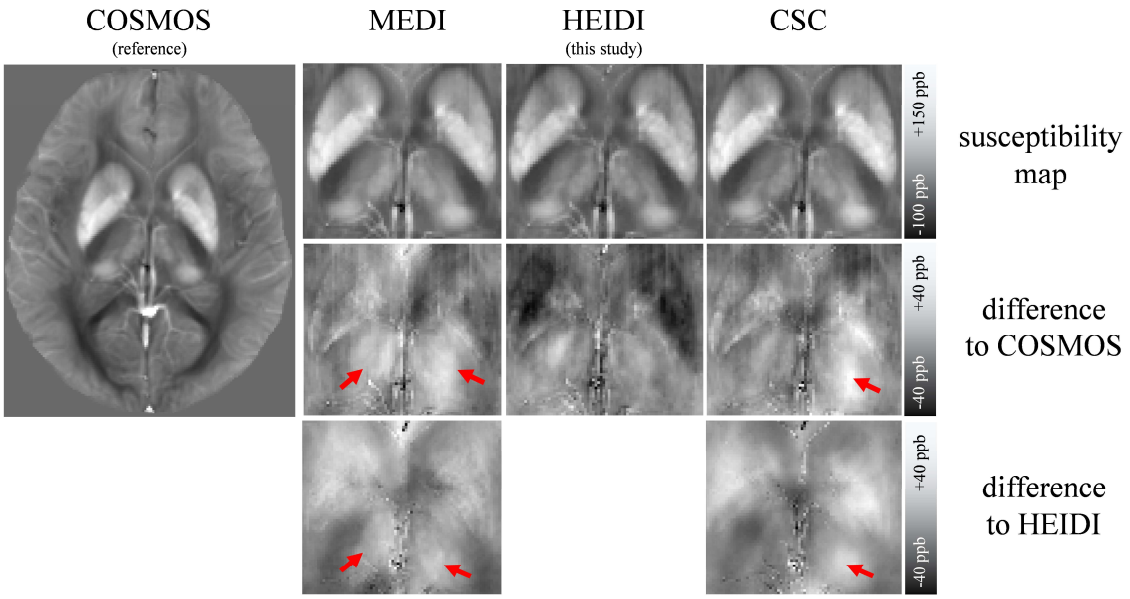

Figure S.7. Comparison of the susceptibility reconstruction accuracy of different QSM algorithms in the thalamus based on the dataset generously provided by the Cornell MRI Research Lab (Yi Wang) at the Weill Cornell Medical College, NY. The dataset analyzed in this figure was used in a recent overview paper (Wang and Liu, 2015) and is available for download on the lab's website. The COSMOS algorithm (left), which relies on field maps acquired with the head at several different orientations relative to the main magnetic field, is commonly regarded as an *in vivo* gold standard. The MEDI algorithm (second from left) uses magnitude-derived anatomical priors for the susceptibility map calculation. The HEIDI algorithm (third from left) was used in the present study. The CS-compensated (CSC) algorithm (Wu et al., 2011) employs a CS-type approach without anatomical priors. The top row shows the susceptibility maps calculated with the individual algorithms. The middle row shows the differences relative to the gold-standard COSMOS susceptibility map. The bottom row shows the differences relative to the HEIDI susceptibility map. While providing accurate estimates of striatal susceptibility values, MEDI calculated substantially higher susceptibility values in the thalamus than COSMOS and HEIDI (red arrows), with clearly visible bi-hemispheric thalamic anatomy in the difference images. HEIDI had the lowest error in the thalamus, with only minor inhomogeneities in the difference image, but striatal susceptibility values were underestimated. The CSC algorithm ranked between HEIDI and MEDI. All images are mean value projections across the 17 slices covering the thalamus.

References

Abdul-Rahman, H. S., Gdeisat, M. A., Burton, D. R., Lalor, M. J., Lilley, F., Moore, C. J., sep 2007. Fast and robust three-dimensional best path phase unwrapping algorithm. Appl Opt 46 (26), 6623–35. http://www.ncbi.nlm.nih.gov/pubmed/17846656

Al-Radaideh, A. M., Wharton, S. J., Lim, S.-Y., Tench, C. R., Morgan, P. S., Bowtell, R. W., Constantinescu, C. S., Gowland, P. a., jun 2013. Increased iron accumulation occurs in the earliest stages of demyelinating disease: an ultra-high field susceptibility mapping study in Clinically Isolated Syndrome. Mult Scler 19 (7), 896–903. http://-www.ncbi.nlm.nih.gov/pubmed/23139386

Bilgic, B., Pfefferbaum, A., Rohlfing, T., Sullivan, E. V., Adalsteinsson, E., feb 2012. MRI estimates of brain iron concentration in normal aging using quantitative susceptibility mapping. NeuroImage 59 (3), 2625–2635. http://www.ncbi.nlm.nih.gov/pubmed/-21925274 http://www.pubmedcentral.nih.gov/-articlerender.fcgi?artid=3254708&tool=pmcentrez&rendertype=abstract http://-linkinghub.elsevier.com/retrieve/pii/S1053811911010093

Burgetova, A., Dusek, P., Vaneckova, M., Horakova, D., Langkammer, C., Krasensky, J., Sobisek, L., Matras, P., Masek, M., Seidl, Z., 2017. Thalamic Iron Differentiates Primary-Progressive and Relapsing-Remitting Multiple Sclerosis. American Journal of Neuroradiology. http://www.ajnr.org/lookup/doi/10.3174/ajnr.A5166

Charil, A., Yousry, T. A., Rovaris, M., Barkhof, F., De Stefano, N., Fazekas, F., Miller, D. H., Montalban, X., Simon, J. H., Polman, C. H., Filippi, M., oct 2006. MRI and the diagnosis of multiple sclerosis: expanding the concept of "no better explanation". Lancet Neurol 5 (10), 841–52. http://www.ncbi.nlm.nih.gov/pubmed/16987731

Chen, W., Gauthier, S. a., Gupta, A., Comunale, J., Liu, T., Wang, S., Pei, M., Pitt, D., Wang, Y., apr 2014. Quantitative Susceptibility Mapping of Multiple Sclerosis Lesions at Various Ages. Radiology 271 (1), 183–192. http://www.ncbi.nlm.nih.gov/pubmed/-24475808 http://pubs.rsna.org/doi/10.1148/radiol.13130353

Cheng, G., Kong, R. H., Zhang, L. M., Zhang, J. N., 2012. Mitochondria in traumatic brain injury and mitochondrial-targeted multipotential therapeutic strategies. British Journal of Pharmacology 167 (4), 699–719.

Contreras, L., Drago, I., Zampese, E., Pozzan, T., 2010. Mitochondria: The calcium connection. Biochimica et Biophysica Acta - Bioenergetics 1797 (6-7), 607–618. http://dx.doi.org/10.1016/j.bbabio.2010.05.005

Deistung, A., Schäfer, A., Schweser, F., Biedermann, U., Turner, R., Reichenbach, J. R., jan 2013. Toward in vivo histology: a comparison of quantitative susceptibility mapping (QSM) with magnitude-, phase-, and R2*-imaging at ultra-high magnetic field strength. NeuroImage 65, 299–314. http://www.ncbi.nlm.nih.gov/pubmed/23036448

Elkady, A. M., Sun, H., Wilman, A. H., 2015. Importance of extended spatial coverage for quantitative susceptibility mapping of iron-rich deep grey matter. Magnetic resonance imaging 34 (4), 574–578. http://linkinghub.elsevier.com/retrieve/pii/-S0730725X15003367%5Cnhttp://www.ncbi.nlm.nih.gov/pubmed/26721523

Feng, X., Deistung, A., Reichenbach, J. R., jun 2017. Quantitative susceptibility mapping (QSM) and R2* in the human brain at 3 T. Z Med Phys. http://-linkinghub.elsevier.com/retrieve/pii/S0939388916301143

Hagemeier, J., Zivadinov, R., Dwyer, M. G., Polak, P., Bergsland, N. P., Weinstock-Guttman, B., Zalis, J., Deistung, A., Reichenbach, J. R., Schweser, F., apr 2017. Changes of deep gray matter magnetic susceptibility over 2 years in multiple sclerosis and healthy control brain. NeuroImage: Clinical, (epub). http://linkinghub.elsevier.com/retrieve/-pii/S2213158217300840

Hallgren, B., Sourander, P., 1958. The effect of age on the non-haemin iron in the human brain. J Neurochem 3, 41–51.

Hammond, K. E., Lupo, J. M., Xu, D., Metcalf, M., Kelley, D. A. C., Pelletier, D., Chang, S. M., Mukherjee, P., Vigneron, D. B., Nelson, S. J., feb 2008. Development of a robust method for generating 7.0 T multichannel phase images of the brain with application to normal volunteers and patients with neurological diseases. NeuroImage 39 (4), 1682–1692. http://dx.doi.org/10.1016/j.neuroimage.2007.10.037

Harrison, D. M., Li, X., Liu, H., Jones, C. K., Caffo, B., Calabresi, P. A., van Zijl, P. C. M., aug 2016. Lesion Heterogeneity on High-Field Susceptibility MRI Is Associated with Multiple Sclerosis Severity. Am J Neuroradiol 37 (8), 1447–1453. http://-www.ajnr.org/cgi/doi/10.3174/ajnr.A4726

Langkammer, C., Bredies, K., Poser, B. A., Barth, M., Reishofer, G., Fan, A. P., Bilgic, B., Fazekas, F., Mainero, C., Ropele, S., 2015. Fast quantitative susceptibility mapping

using 3D EPI and total generalized variation. NeuroImage 111 (February 2016), 622–630.

Lassmann, H., van Horssen, J., Mahad, D., sep 2012. Progressive multiple sclerosis: pathology and pathogenesis. Nature Reviews Neurology 8 (11), 647–656. http://-www.nature.com/doifinder/10.1038/nrneurol.2012.168

Li, W., Wu, B., Liu, C., apr 2011. Quantitative susceptibility mapping of human brain reflects spatial variation in tissue composition. NeuroImage 55 (4), 1645–56. http://-www.pubmedcentral.nih.gov/-articlerender.fcgi?artid=3062654&tool=pmcentrez&rendertype=abstract

Li, X., Harrison, D. M., Liu, H., Jones, C. K., Oh, J., Calabresi, P. A., van Zijl, P. C. M., feb 2016. Magnetic susceptibility contrast variations in multiple sclerosis lesions. J Magn Reson Imaging 43 (2), 463–473. http://doi.wiley.com/10.1002/jmri.24976

Moore, D. F., Ye, F., Schiffmann, R., Butman, J. a., 2003. Increased signal intensity in the pulvinar on T1-weighted images: a pathognomonic MR imaging sign of Fabry disease. Am J Roentgenol 24 (6), 1096–101. http://www.ncbi.nlm.nih.gov/pubmed/12812932

Osteen, C. L., Giza, C. C., Hovda, D. A., 2004. Injury-induced alterations in N-methyl-D-aspartate receptor subunit composition contribute to prolonged 45calcium accumulation following lateral fluid percussion. Neuroscience 128 (2), 305–322.

Osteen, C. L., Moore, A. H., Prins, M. L., Hovda, D. A., 2001. Age-dependency of 45calcium accumulation following lateral fluid percussion: acute and delayed patterns. J Neurotrauma 18 (2), 141–62. http://www.ncbi.nlm.nih.gov/pubmed/11229708

Panov, A. V., Andreeva, L., Greenamyre, J. T., 2004. Quantitative evaluation of the effects of mitochondrial permeability transition pore modifiers on accumulation of calcium phosphate: Comparison of rat liver and brain mitochondria. Archives of Biochemistry and Biophysics 424 (1), 44–52.

Polak, P., Zivadinov, R., Schweser, F., 2015. Gradient Unwarping for Phase Imaging Reconstruction. In: Proc Intl Soc Mag Reson Med 23 (2015). Toronto, CA, p. 1279.

Ramcharan, E. J., Gnadt, J. W., Sherman, S. M., 2005. Higher-order thalamic relays burst more than first-order relays. Proceedings of the National Academy of Sciences of the United States of America 102 (34), 12236–41. http://www.pubmedcentral.nih.gov/-articlerender.fcgi?artid=1189315&tool=pmcentrez&rendertype=abstract

Rudko, D. A., Solovey, I., Gati, J. S., Kremenchutzky, M., Menon, R. S., sep 2014. Multiple Sclerosis: Improved Identification of Disease-relevant Changes in Gray and White Matter by Using Susceptibility-based MR Imaging. Radiology 272 (3), 851–864. http://pubs.rsna.org/doi/full/10.1148/radiol.14132475 http://pubs.rsna.org/doi/abs/-10.1148/radiol.14132475

Schweser, F., Deistung, A., Lehr, B. W., Reichenbach, J. R., oct 2011. Quantitative imaging of intrinsic magnetic tissue properties using MRI signal phase: An approach to in vivo brain iron metabolism? NeuroImage 54 (4), 2789–2807. http://-www.ncbi.nlm.nih.gov/pubmed/21040794 http://dx.doi.org/10.1016/-j.neuroimage.2010.10.070

Schweser, F., Poulsen, A., Shah, D., Bertolino, N., Preda, M., Kyyriäinen, J., Pitkänen, A., Zivadinov, R., Poulsen, D. J., 2017. 9.4 Tesla in vivo Quantitative Susceptibility Mapping (QSM) detects thalamic calcium influx associated with repeated mild traumatic brain injury (mTBI). In: Proc Intl Soc Mag Reson Med 25 (2017). Honolulu, HI.

Schweser, F., Sommer, K., Deistung, A., Reichenbach, J. R., jun 2012. Quantitative susceptibility mapping for investigating subtle susceptibility variations in the human brain. NeuroImage 62 (3), 2083–2100. http://linkinghub.elsevier.com/retrieve/pii/-S1053811912005551 http://www.ncbi.nlm.nih.gov/pubmed/22659482

Sherman, S. M., Guillery, R. W., 2013. First and Higher Order Thalamic Relays. In: Functional Connections of Cortical Areas: A New View from the Thalamus. MIT Press, Ch. 5.4.2.2, pp. 119–141.

Straub, S., Schneider, T. M., Emmerich, J., Freitag, M. T., Ziener, C. H., Schlemmer, H.-p., Ladd, M. E., Laun, F. B., aug 2016. Suitable reference tissues for quantitative susceptibility mapping of the brain. Magnetic Resonance in Medicine 00 (9), 3–6. http://doi.wiley.com/10.1002/mrm.26369

Strijbis, E. M. M., Inkster, B., Vounou, M., Naegelin, Y., Kappos, L., Radue, E.-W., Matthews, P. M., Uitdehaag, B. M. J., Barkhof, F., Polman, C. H., Montana, G., Geurts, J. J. G., 2013. Glutamate gene polymorphisms predict brain volumes in multiple sclerosis. Multiple sclerosis (Houndmills, Basingstoke, England) 19 (3), 281–8. http://www.ncbi.nlm.nih.gov/pubmed/22851457

Wang, Y., Liu, T., 2015. Quantitative susceptibility mapping (QSM): Decoding MRI data for a tissue magnetic biomarker. Magn Reson Med 73 (1), 82–101. http://doi.wiley.com/-10.1002/mrm.25358

Wei, H., Bonjean, M., Petry, H. M., Sejnowski, T. J., Bickford, M. E., 2011. Thalamic Burst Firing Propensity: A Comparison of the Dorsal Lateral Geniculate and Pulvinar Nuclei in the Tree Shrew. Journal of Neuroscience 31 (47), 17287–17299.

Wu, B., Li, W., Guidon, A., Liu, C., 2011. Whole brain susceptibility mapping using compressed sensing. Magn Reson Med 24, 1129–36. http://www.ncbi.nlm.nih.gov/-pubmed/21671269

Zhou, Q., Godwin, D. W., O'Malley, D. M., Adams, P. R., 1997. Visualization of calcium influx through channels that shape the burst and tonic firing modes of thalamic relay cells. Journal of neurophysiology 77 (5), 2816–2825. http://www.ncbi.nlm.nih.gov/-pubmed/9163395%5Cnhttp://jn.physiology.org/content/77/5/2816.short

Zivadinov, R., Schirda, C., Dwyer, M. G., Haacke, E. M., Weinstock-Guttman, B., Menegatti, E., Heininen-Brown, M., Magnano, C. R., Malagoni, a. M., Wack, D. S., Hojnacki, D., Kennedy, C., Carl, E., Bergsland, N. P., Hussein, S., Poloni, G. U., Bartolomei, I., Salvi, F., Zamboni, P., apr 2010. Chronic cerebrospinal venous insufficiency and iron deposition on susceptibility-weighted imaging in patients with multiple sclerosis: a pilot case-control study. Int Angiol 29 (2), 158–75. http://www.ncbi.nlm.nih.gov/-pubmed/20351672